

KINEMATIC ANALYSES OF A NEW MEDICAL ROBOT FOR 3D VASCULAR ULTRASOUND EXAMINATION

Longfei Zhao, Andy Kar Wah Yen, Jonathan Coulombe, Pascal Bigras, and Ilian A. Bonev
École de technologie supérieure, Montreal, QC, Canada
pascal.bigras@etsmtl.com

ABSTRACT

Peripheral artery disease (PAD) is a common vascular disease which can have serious consequences for older people. Owing to the complexity of the vessels in the lower limbs, current PAD medical robots are not desirable to diagnose PAD in this area. The kinematic model of a novel six-axis serial-parallel robot for 3D vascular ultrasound examination of the lower limbs is presented in this paper. The prototype of the robot is described, and then the direct and inverse kinematic problems are solved in closed form.

Keywords: serial-parallel robot; medical robot; kinematics.

MODÈLE GÉOMÉTRIQUE D'UN NOUVEAU ROBOT MÉDICAL D'IMAGERIE 3D PAR ULTRASON

RÉSUMÉ

La maladie occlusive artérielle périphérique affecte une partie importante de la population d'âge mûr. Les robots développés pour caractériser cette maladie ne sont actuellement pas adaptés aux membres inférieurs en raison de la longueur et de la complexité du groupe d'artères concerné. Cet article présente le modèle géométrique d'un nouveau robot sériel-parallèle conçu spécialement pour l'échographie tridimensionnelle des membres inférieurs. Le prototype est d'abord présenté. Puis, les modèles géométriques directe et inverse sont expliqués en détail.

Mots-clés : robot série-parallèle ; robot médical ; modèle géométrique.

1 INTRODUCTION

Peripheral arterial disease (PAD) is a very common, but serious disease that occurs in the lower limbs. It narrows, and can even block, the vessels that carry blood from the heart to the limbs [1]. According to [2], the prevalence of PAD of a group over 70 years old is nearly 15%, but only 10% of them have observable symptoms. If PAD is not detected and diagnosed in time, patients will suffer intermittent claudication, and the limb may even require amputation [3]. Medical imaging techniques are generally used in the diagnosis of PAD to precisely locate blockages, or occlusions, and characterize their morphological features. Among the most common of these techniques, which include angiography, ultrasound scan, computed tomography angiography (CTA), and magnetic resonance angiography (MRA), ultrasound scan far outweighs the others due to its non-radiation lower cost [4].

Several handheld medical robots have been developed for PAD diagnosis using ultrasound imaging, such as TERESA [5,6] and OTELO [7,8]. This type of PAD robot requires quite a small workspace, and should be held by the technician during operation. A survey of 232 sonographers [9] has revealed that the repetitive strain of carrying this load over many working hours leads to musculoskeletal disorders. Several other robots have been developed for ultrasound imaging of the abdominal area, such as Ehime University's robot [10,11] and a cable robot, TER [12]. However, this area is flatter for ultrasound scan purposes than a leg, and the geometric design of these robots indicates that they are unsuitable for examining the lower limbs. The Hippocrate robot in France [13] and the fully statically balanced medical robot at the University of British Columbia [14] are designed for PAD diagnosis in the carotid area, where the artery concerned is fairly short and straight. Finally, in [15], we propose a new serial-parallel robot architecture for PAD diagnosis in the lower limbs, where blood vessels are long, complex, and twisted. That paper presents the architecture and a static balancing optimization for this robot, but its kinematic model is not analyzed, nor is its prototype presented.

This paper presents hardware setup and a detailed kinematic analysis of the new medical robot (MedRUE), which is based on the architecture proposed in [15]. MedRUE (Medical Robot for vascular Ultrasound Examination) is suitable for lower limb PAD diagnosis (Fig. 1a), and the workspace covers the entire lower limb area that needs to be scanned. Moreover, the robot has sufficient dexterity to insert and rotate a probe in the narrow space of a lower limb. The remaining sections are organized as follows. In section 2, the robot specifications and setup are discussed in detail. In sections 3 and 4, we present the direct and inverse kinematics of MedRUE respectively. In section 5, we address the singularity issues. Our conclusions are given in section 6.

2 ROBOT ARCHITECTURE AND HARDWARE SETUP

MedRUE has a patented serial-parallel architecture [16] designed to follow the complex and twisted structure of the artery in lower limbs. It can be regarded as comprising four components: a mobile base, two five-bar mechanisms, and a tool part (Fig. 1b).

The mobile base is attached to the carriage of a LinTech 150 series linear guide. This allows MedRUE to translate along the x_0 axis off the base frame O_0 , and it covers the length of a typical lower limb. This decoupled design has made it possible to minimize MedRUE's dimensions. Furthermore, because four of its six motors are mounted on the mobile base, the rest of the robot is relatively light and nimble.

The two symmetrical five-bar mechanisms are attached to the mobile base. They work in parallel planes perpendicular to the direction of the base linear guide. The combined motion of these two mechanisms enables the translation and orientation of the ultrasound probe along the y_0 and z_0 axes.

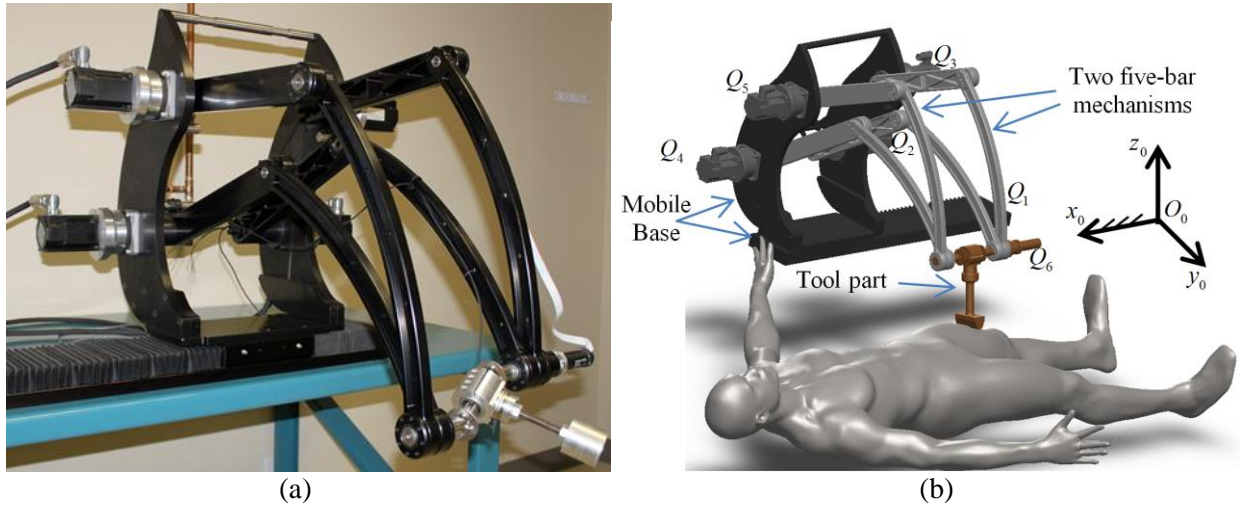


Fig. 1. (a) MedRUE robot; (b) CAD model.

The tool part connects the extremities of the two five-bar mechanisms through two passive universal joints. A passive prismatic joint is located between the two universal joints to compensate for the change in distance between the two extremities of the five-bar mechanisms. A small motor is located on one of the mechanisms to drive the rotation of the tool part.

The general specifications of the main components of MedRUE are listed in Table 1. We have verified with simulations in [17] that, under these specifications the workspace of MedRUE can cover the area on the lower limbs that requires scan. The main components are made of aluminum alloy 6061-T6, and the shafts and pins are fabricated with alloy steel 4140.

Table 1. Specifications of the Main Components

	Mass	Length	Other features
Robot	45 kg	0.91 m (linear guide)	Full extension: 0.92 m
Five-bar mechanism links			
actuated bars	0.68 kg	0.40 m	Inertia: 0.013 kg·m ²
passive bars	0.82 kg	0.52 m	Inertia: 0.024 kg·m ²
Tool part			
Telescoping double universal joint	0.90 kg	0.080 m	Radius: 0.030 m
force sensor and ultrasound probe	0.50 kg	0.18 m	Radius: 0.020 m

The motors and drivers that were selected are listed in Table 2. The selection criterion mainly takes into account size, precision, and nominal speed. A Mini40 force/torque sensor from ATI is attached between the ultrasound probe (only a dummy probe is shown in Fig. 1a) and the tool flange of the robot. Although it is small (a radius of 0.02 m and a height of 0.014 m), it can measure forces up to 60 N and torques up to 1 Nm. This is sufficient in our application, since the normal force during ultrasound examination is typically below 30 N and the torques are much smaller than 1 Nm.

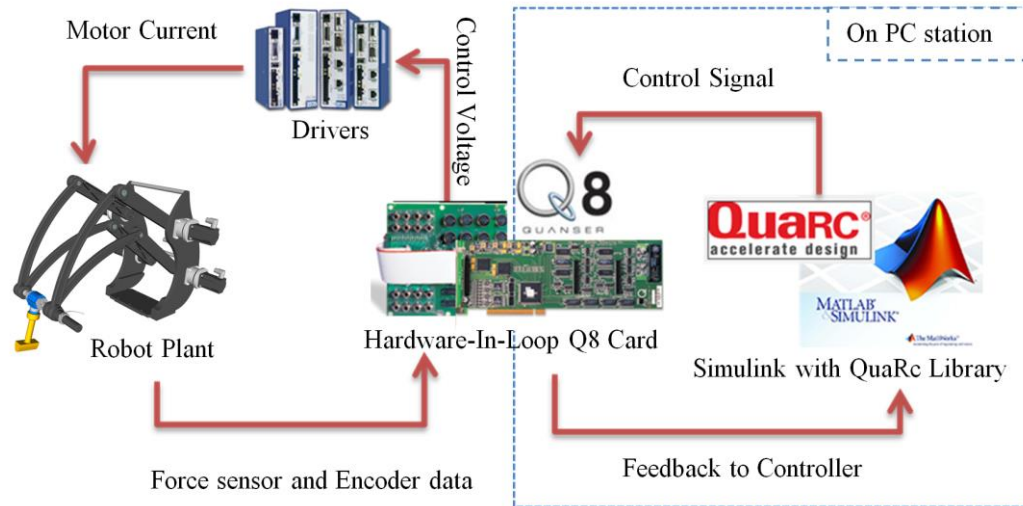


Fig. 2. Setup of MedRUE.

Figure 2 shows the setup of the robot system. A Q8 I/O card from Quanser provides eight A/D ports, eight D/A ports, eight encoder inputs, and thirty two digital I/O ports. Six A/D ports are used for reading the force/torque sensor data, and six encoder inputs are used for position data. On a PC station, these sensor data can be read and serve as feedback for the robot controller using the Quanser library QuaRC in Simulink. A real-time thread is created by QuaRC to run the program code generated by Simulink. While MedRUE is moving, the user can start/stop the program or modify/observe the controller's parameters. The Q8 card sends the control command from six D/A ports to drivers to generate torques of six motors on the robot.

Table 2. MedRUE Motors and Drivers

Actuators	Q_1	Q_2, Q_3, Q_4, Q_5	Q_6
Drivers	Danher S20660VTS	Danaher S20260VTS	Maxon ADS 50/5
Servomotors	Kollmorgen AKM42G	Kollmorgen AKM31E	Maxon 31007SP
Mass	3.4 kg	1.6 kg	0.24 kg
Inertia	$1.5 \times 10^{-4} \text{ kg.m}^2$	$0.33 \times 10^{-4} \text{ kg.m}^2$	$0.033 \times 10^{-4} \text{ kg.m}^2$
Gear box	LinTech 150836-WC1-1-S129-M04	HD CSF-20-80	HD CSF-08-50
Gear ratio	$100 \pi \text{ rad: } 1 \text{ m}$	80:1	50:1

3 DIRECT KINEMATIC MODEL

A geometric approach based on MedRUE's four components is used to find its direct kinematic model. First, a kinematic model of a general five-bar mechanism is analyzed, and its results are then adapted to MedRUE's kinematic model.

Five-bar mechanism

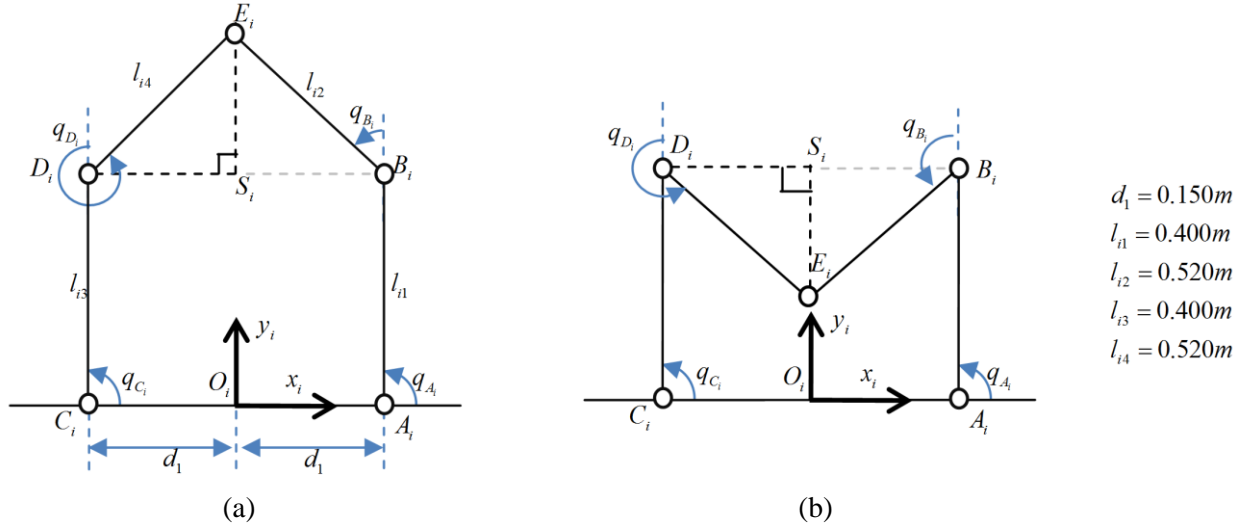


Fig. 3. General five-bar mechanism: (a) positive assembly mode; (b) negative assembly mode.

Figure 3 shows a general five-bar mechanism in the $x_i y_i$ plane of the frame O_i ($i = 1, 2$, throughout this paper) in two assembly modes. The link $A_i C_i$ with length $2d_1$ is fixed with the x_i axis of frame O_i , while other four links can rotate with axes located at their geometric ends. Lengths of four movable links are denoted as l_{ij} where $j = 1$ to 4. Variables q_{A_i} and q_{C_i} are the values of the actuated revolute joints, while q_{B_i} and q_{D_i} are passive revolute joints values. E_i is considered as the end point of this mechanism.

The vectors from the origin point O_i to A_i and C_i are represented as

$$\mathbf{r}_{O_i A_i} = \begin{bmatrix} x_{O_i A_i} & y_{O_i A_i} & z_{O_i A_i} \end{bmatrix}^T = \begin{bmatrix} d_1 & 0 & 0 \end{bmatrix}^T, \quad (1)$$

$$\mathbf{r}_{O_i C_i} = \begin{bmatrix} x_{O_i C_i} & y_{O_i C_i} & z_{O_i C_i} \end{bmatrix}^T = \begin{bmatrix} -d_1 & 0 & 0 \end{bmatrix}^T, \quad (2)$$

Thus the vectors from the origin point O_i to B_i and D_i are obtained as

$$\mathbf{r}_{O_i B_i}(q_{A_i}) = \begin{bmatrix} x_{O_i A_i} + l_{11} \cos q_{A_i} \\ y_{O_i A_i} + l_{11} \sin q_{A_i} \\ 0 \end{bmatrix}, \quad (3)$$

$$\mathbf{r}_{O_i D_i}(q_{C_i}) = \begin{bmatrix} x_{O_i C_i} + l_{13} \cos q_{C_i} \\ y_{O_i C_i} + l_{13} \sin q_{C_i} \\ 0 \end{bmatrix}. \quad (4)$$

As shown in Fig. 3, S_i is defined as the projection of E_i on the vector $\mathbf{r}_{D_i B_i} = \mathbf{r}_{O_i B_i} - \mathbf{r}_{O_i D_i}$. If $\|\mathbf{r}_{D_i B_i}\| = \sqrt{\mathbf{r}_{D_i B_i}^T \mathbf{r}_{D_i B_i}} > l_{14} + l_{12}$, there will be no solution, since the distance between q_{A_i} and q_{C_i} exceeds the sum of the link lengths. Otherwise, applying the Pythagorean theorem on the two right triangles $D_i S_i E_i$ and $B_i S_i E_i$, we have:

$$\left. \begin{aligned} \|\mathbf{r}_{S_i E_i}\|^2 + \|\mathbf{r}_{D_i S_i}\|^2 &= l_{i4}^2 \\ \|\mathbf{r}_{S_i E_i}\|^2 + \left(\|\mathbf{r}_{D_i B_i}\| - \|\mathbf{r}_{D_i S_i}\| \right)^2 &= l_{i2}^2 \end{aligned} \right\}. \quad (5)$$

Equation (5) gives the solution:

$$\left. \begin{aligned} \mathbf{r}_{D_i S_i}(q_{A_i}, q_{C_i}) &= \frac{l_{i4}^2 - l_{i2}^2 + \|\mathbf{r}_{D_i B_i}\|^2}{2\|\mathbf{r}_{D_i B_i}\|} \frac{\mathbf{r}_{D_i B_i}}{\|\mathbf{r}_{D_i B_i}\|} \\ \mathbf{r}_{S_i E_i}(q_{A_i}, q_{C_i}) &= \sqrt{l_{i4}^2 - \|\mathbf{r}_{D_i S_i}\|^2} \begin{bmatrix} 0 & -1 & 0 \\ 1 & 0 & 0 \\ 0 & 0 & 0 \end{bmatrix} \frac{\mathbf{r}_{D_i B_i}}{\|\mathbf{r}_{D_i B_i}\|} \end{aligned} \right\}. \quad (6)$$

The solution for the end point E_i is

$$\mathbf{r}_{O_i E_i}(q_{A_i}, q_{C_i}) = \mathbf{r}_{O_i D_i} + \mathbf{r}_{D_i S_i} \pm \mathbf{r}_{S_i E_i}. \quad (7)$$

The sign in front of vector $\mathbf{r}_{S_i E_i}$ is positive if the mechanism is in positive assembly mode, as indicated in Fig. 3a, and negative when in negative assembly mode, as shown in Fig. 3b. The five-bar mechanism in MedRUE is the first case.

Then, the angle values of the passive joints are

$$q_{B_i} = \text{atan2}(y_{O_i E_i} - y_{O_i B_i}, x_{O_i E_i} - x_{O_i B_i}) - q_{A_i}, \quad (8)$$

$$q_{D_i} = \text{atan2}(y_{O_i E_i} - y_{O_i D_i}, x_{O_i E_i} - x_{O_i D_i}) - q_{C_i}. \quad (9)$$

MedRUE

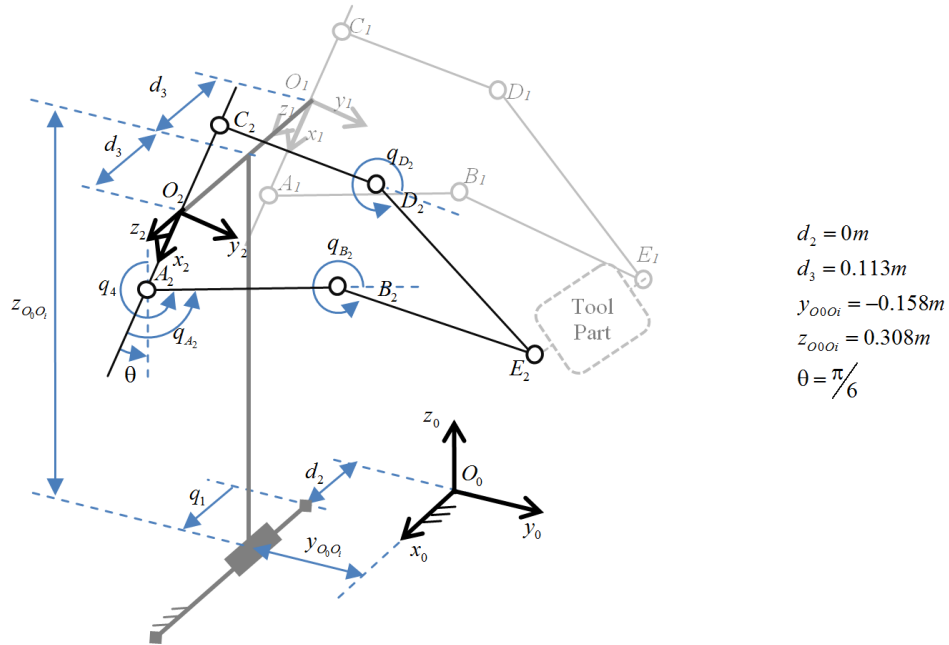


Fig. 4. MedRUE architecture.

If the five-bar mechanism in Fig. 4 is rotated around the z_i axis at a constant angle of $-(\theta + \pi/2)$, and then duplicated onto the mobile base, the architecture of MedRUE in Fig. 1b can be redrawn as in Fig. 4. It is notable that both q_{B_i} and q_{D_i} in Fig. 4 are always greater than π rad, for providing space for patients under the robot arms. The two five-bar planes are parallel and perpendicular to the x_0 axis of the base frame O_0 . Referring to the definition of q_4 in Fig. 4, four actuated revolute joint values are defined as

$$q_4 = \pi - \theta + q_{A_2}, q_5 = \pi - \theta + q_{C_2}, q_2 = \pi - \theta + q_{A_1}, q_3 = \pi - \theta + q_{C_1}. \quad (10)$$

The homogeneous transformation matrix of the frames O_i w.r.t. the base frame O_0 is

$${}^0\mathbf{T}_i(\theta) = \mathbf{D}_x(x_{0_0O_i})\mathbf{D}_y(y_{0_0O_i})\mathbf{D}_z(z_{0_0O_i})\mathbf{R}_y\left(\frac{\pi}{2}\right)\mathbf{R}_z(-\theta) = \begin{bmatrix} 0 & 0 & 1 & x_{0_0O_i} \\ -\sin(\theta) & \cos(\theta) & 0 & y_{0_0O_i} \\ -\cos(\theta) & -\sin(\theta) & 0 & z_{0_0O_i} \\ 0 & 0 & 0 & 1 \end{bmatrix}, \quad (11)$$

where $x_{0_0O_i} = d_2 + q_1 + (-1)^i d_3$.

The coordinates of E_i can be represented in the base frame by parameters defined in (10), combined with the five-bar model (7) and transformation (11):

$$\mathbf{r}_{O_0E_1}(q_2, q_3) = {}^0\mathbf{T}_1\mathbf{r}_{O_1E_1}(q_{A_1}, q_{C_1}), \quad (12)$$

$$\mathbf{r}_{O_0E_2}(q_4, q_5) = {}^0\mathbf{T}_2\mathbf{r}_{O_2E_2}(q_{A_2}, q_{C_2}). \quad (13)$$

As shown in Fig. 5a, the coordinates of the universal joint centers are

$$\mathbf{r}_{O_0E_1}(q_2, q_3) = \mathbf{r}_{O_0E_1}(q_2, q_3) + [d_4 \ 0 \ 0]^T, \quad (14)$$

$$\mathbf{r}_{O_0E_2}(q_4, q_5) = \mathbf{r}_{O_0E_2}(q_4, q_5) - [d_4 \ 0 \ 0]^T. \quad (15)$$

The dashed box in Fig. 5b demonstrates the physical revolution sequence of the tool part: rotation along the temporal axes x' , y' , and z' . Owing to the mechanical design of the tool part, x' always aligns with x_0 , and z' with z_p . As defined in Fig. 5b, when $\alpha = \beta = \gamma = 0$, then x' , y' , and z' align with the corresponding axes of the base frame.

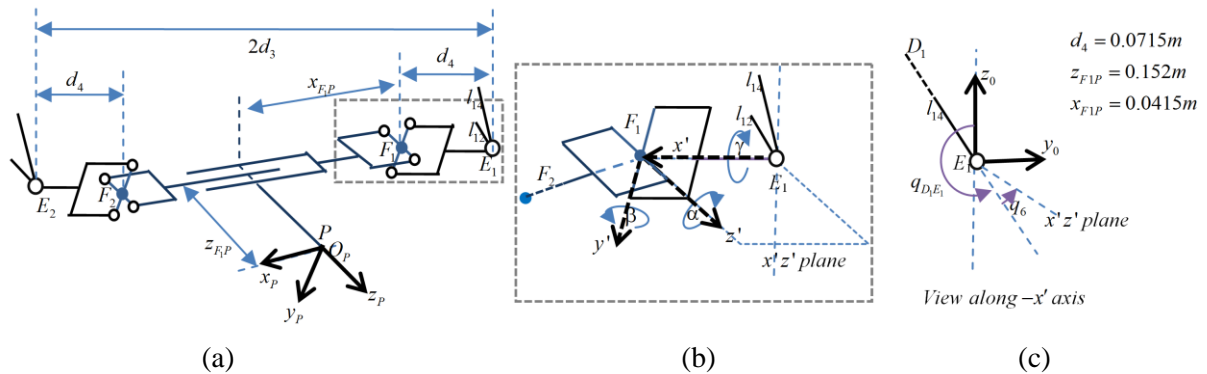


Fig. 5. Architecture of the MedRUE tool part: (a) overall structure; (b) microscopic view of the dashed block in (a); (c) view on (b) from right to left.

Confirming the revolution sequence of the tool part, Euler-XYZ angles [18] are chosen to express the orientation of the tool tip frame O_p w.r.t. the base frame O_0 . In this context, γ is the sum of the rotations along x' (in Fig. 5c), and can be obtained by

$$\gamma = q_{D_1E_1} + q_6 \quad (16)$$

where $q_{D_1E_1} = \text{atan2}\left(-\left(y_{O_0E_1} - y_{O_0D_1}\right), z_{O_0E_1} - z_{O_0D_1}\right)$.

Actuator Q_6 is fixed on l_{14} between D_1 and E_1 , and so q_6 is defined as the angle starting from l_{14} to the $x'z'$ plane. Since the probe will always point down to the skin surface during the scan process, γ is restrained in the open interval $\left(\frac{\pi}{2}, \frac{3\pi}{2}\right)$.

The unit vector from F_1 to F_2 aligns with the x_p axis of the frame O_p , yielding

$$\mathbf{u}_{F_1F_2} = \mathbf{R}_x(\gamma)\mathbf{R}_y(\beta)\mathbf{R}_z(\alpha)\begin{bmatrix} 1 & 0 & 0 \end{bmatrix}^T = \begin{bmatrix} \cos\beta\cos\alpha \\ \sin\gamma\sin\beta\cos\alpha + \cos\gamma\sin\alpha \\ -\cos\gamma\sin\beta\cos\alpha + \sin\gamma\sin\alpha \end{bmatrix}. \quad (17)$$

Equation (17) can also be represented by variables defined in (14) and (15):

$$\mathbf{u}_{F_1F_2} = \frac{\mathbf{r}_{O_0F_2} - \mathbf{r}_{O_0F_1}}{\|\mathbf{r}_{O_0F_2} - \mathbf{r}_{O_0F_1}\|} = \begin{bmatrix} u_x \\ u_y \\ u_z \end{bmatrix}. \quad (18)$$

If it were assumed that $|\alpha|, |\beta|$ can reach $\frac{\pi}{2}$, then $x_{O_0F_1}$ would be equal to $x_{O_0F_2}$ in Fig. 5. This is impossible, because F_1 and F_2 are rigidly attached to the two parallel five-bar mechanisms, and the distance between F_1 and F_2 along the x_0 axis is a constant:

$$u_x \|\mathbf{r}_{O_0F_2} - \mathbf{r}_{O_0F_1}\| = x_{O_0F_2} - x_{O_0F_1} = 2(d_3 - d_4). \quad (19)$$

Thus, the inequalities $|\alpha| < \frac{\pi}{2}$ and $|\beta| < \frac{\pi}{2}$ must stand, and $\cos\alpha \neq 0$ in (17). In the design of MedRUE, the mechanical limit of a universal joint is $|\alpha| \leq \frac{\pi}{6}, |\beta| \leq \frac{\pi}{6}$. Then, α and β can be computed by (17) and (18):

$$\alpha = \sin^{-1}(u_y \cos\gamma + u_z \sin\gamma), \quad (20)$$

$$\beta = \sin^{-1}\left(\frac{u_y \sin\gamma - u_z \cos\gamma}{\cos\alpha}\right). \quad (21)$$

The coordinates of the probe tip P can be represented by

$$\mathbf{r}_{O_0P} = \mathbf{r}_{O_0F_1} + {}^0\mathbf{T}_P \mathbf{r}_{F_1P}, \quad (22)$$

where $\mathbf{r}_{F_1P} = [x_{F_1P}, 0, z_{F_1P}]^T$ is a constant vector in Fig. 5a. The homogeneous transformation matrix of the

frame O_p w.r.t. O_0 is ${}^0\mathbf{T}_P = \begin{bmatrix} {}^0\mathbf{R}_P & \mathbf{r}_{O_0P} \\ \mathbf{0} & 0 \end{bmatrix}$, and ${}^0\mathbf{R}_P(\alpha, \beta, \gamma) = \mathbf{R}_x(\gamma)\mathbf{R}_y(\beta)\mathbf{R}_z(\alpha)$.

4 INVERSE KINEMATIC MODEL

The inverse kinematic model will be solved based on the MedRUE components, in the same way that the direct kinematic model was found in the previous section. In this case, the coordinates of E_i are computed based on the features of the tool part, and then be transformed into the local frames O_i of five-bar mechanisms. Finally, all the joint values are obtained by solving the inverse kinematic model for a five-bar mechanism.

Given the pose $(x_{O_0P}, y_{O_0P}, z_{O_0P}, \alpha, \beta, \gamma)$ of the tool tip frame O_p , the coordinates of F_1 can be obtained by inverting (22):

$$\mathbf{r}_{O_0F_1} = \mathbf{r}_{O_0P} (x_{O_0P}, y_{O_0P}, z_{O_0P}) - \mathbf{R}_x(\gamma) \mathbf{R}_y(\beta) \mathbf{R}_z(\alpha) \mathbf{r}_{F_1P}. \quad (23)$$

To obtain the coordinates of F_2 , (18) can be rewritten as

$$\mathbf{r}_{O_0F_2} = \|\mathbf{r}_{O_0F_2} - \mathbf{r}_{O_0F_1}\| \mathbf{u}_{F_1F_2} + \mathbf{r}_{O_0F_1} \quad (24)$$

where $\mathbf{u}_{F_1F_2}$ can be calculated from (17). By combining (17) and (19), the distance between F_1 and F_2 can be represented as

$$\|\mathbf{r}_{O_0F_2} - \mathbf{r}_{O_0F_1}\| = \frac{2(d_3 - d_4)}{\cos \beta \cos \alpha}. \quad (25)$$

Adding the offsets according to (14) and (15), the end points of the two five-bar mechanisms are

$$\mathbf{r}_{O_0E_i} = \mathbf{r}_{O_0F_i} + (-1)^i [d_4 \quad 0 \quad 0]^T, \quad i=1,2. \quad (26)$$

From (11), the translation joint value is

$$q_1 = x_{O_0O_1} + d_3 - d_2. \quad (27)$$

Since the five-bar mechanism is located in the plane perpendicular to the x_0 axis of frame O_0 , (27) can be rewritten as

$$q_1 = x_{O_0E_1} + d_3 - d_2. \quad (28)$$

With the constant transformation matrix ${}^0\mathbf{T}_i(\theta)$ that we introduced in (11), the coordinates of the end points of the five-bar mechanisms can be represented in their local frame O_i , as in (29). In this way, the rest of the inverse geometric model of the robot is transformed into an inverse geometric model for a five-bar mechanism:

$$\mathbf{r}_{O_iE_i} = {}^0\mathbf{T}_i^{-1} \mathbf{r}_{O_0E_i}, \text{ for } i=1,2. \quad (29)$$

Five-bar mechanism

There will be no solution for q_{A_i} , if $\|\mathbf{r}_{A_iE_i}\| > l_{i1} + l_{i2}$, where $\mathbf{r}_{A_iE_i} = \mathbf{r}_{O_iA_i} - \mathbf{r}_{O_iE_i}$. As shown in Fig. 6, G_i is defined as the projection of B_i on the vector $\mathbf{r}_{A_iE_i} = \mathbf{r}_{O_iE_i} - \mathbf{r}_{O_iA_i}$, and H_i is defined as the projection of D_i on the vector $\mathbf{r}_{C_iE_i} = \mathbf{r}_{O_iE_i} - \mathbf{r}_{O_iC_i}$. Applying the same method used in (5) on both left and right half sides of the five-bar mechanism,

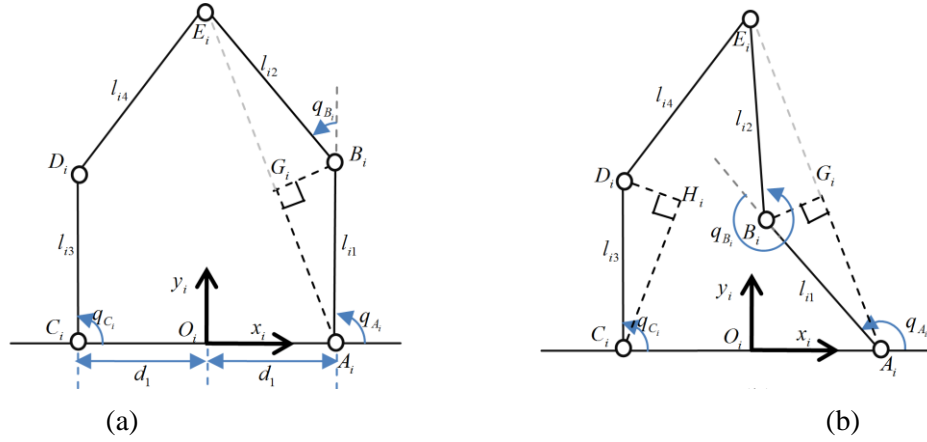


Fig. 6. Two solutions for the inverse kinematic model of a five-bar mechanism.

$$\left. \begin{aligned} \mathbf{r}_{A_i G_i} &= \frac{l_{i1}^2 - l_{i2}^2 + \|\mathbf{r}_{A_i E_i}\|^2}{2\|\mathbf{r}_{A_i E_i}\|} \frac{\mathbf{r}_{A_i E_i}}{\|\mathbf{r}_{A_i E_i}\|} \\ \mathbf{r}_{G_i B_i} &= \sqrt{l_{i1}^2 - \|\mathbf{r}_{A_i G_i}\|^2} \begin{bmatrix} 0 & -1 & 0 \\ 1 & 0 & 0 \\ 0 & 0 & 0 \end{bmatrix} \frac{\mathbf{r}_{A_i E_i}}{\|\mathbf{r}_{A_i E_i}\|} \end{aligned} \right\}, \quad (30)$$

$$\left. \begin{aligned} \mathbf{r}_{C_i H_i} &= \frac{l_{i3}^2 - l_{i4}^2 + \|\mathbf{r}_{C_i E_i}\|^2}{2\|\mathbf{r}_{C_i E_i}\|} \frac{\mathbf{r}_{C_i E_i}}{\|\mathbf{r}_{C_i E_i}\|} \\ \mathbf{r}_{H_i D_i} &= \sqrt{l_{i3}^2 - \|\mathbf{r}_{C_i H_i}\|^2} \begin{bmatrix} 0 & -1 & 0 \\ 1 & 0 & 0 \\ 0 & 0 & 0 \end{bmatrix} \frac{\mathbf{r}_{C_i E_i}}{\|\mathbf{r}_{C_i E_i}\|} \end{aligned} \right\}. \quad (31)$$

Confirming the MedRUE configuration, the vector $\mathbf{r}_{O_i B_i}$ can be obtained by

$$\mathbf{r}_{O_i B_i} = \mathbf{r}_{O_i A_i} + \mathbf{r}_{A_i G_i} \pm \mathbf{r}_{G_i B_i}, \quad (32)$$

$$\mathbf{r}_{O_i D_i} = \mathbf{r}_{O_i C_i} + \mathbf{r}_{C_i H_i} \pm \mathbf{r}_{H_i D_i}. \quad (33)$$

The signs in (32) and (33) demonstrate two different solutions of the configurations of a unit, given the pose of the end points of the five-bar mechanism. The sign is negative when the configuration is as in Fig. 6a, and positive when it is as shown in Fig. 6b. MedRUE always works in the latter case for both five-bar mechanisms. Knowing the coordinates of B_i and D_i , the active joint values can be obtained by

$$q_A = \text{atan2}(y_{O_i B_i} - y_{O_i A_i}, x_{O_i B_i} - x_{O_i A_i}), \quad (34)$$

$$q_{C_i} = \text{atan2}(y_{O_i D_i} - y_{O_i C_i}, x_{O_i D_i} - x_{O_i C_i}). \quad (35)$$

Finally, by submitting the results q_{A_i} and q_{C_i} to (10), we obtain the joint values q_2, q_3, q_4 , and q_5 . The translation joint q_1 is obtained in (28), and the last joint value can be deduced from (9) and (16),

$$q_6 = \gamma - q_3 - q_{D_i}. \quad (36)$$

5 SINGULARITY ISSUES

Singularities only exist in the two five-bar mechanisms of MedRUE. For each mechanism, there are two types of singularity. A Type I singularity occurs when any side of the five-bar mechanism fully extends (Fig. 7a) or overlaps (Fig. 7b). A Type II singularity occurs when two adjacent bars around the end point overlap (Fig. 7c) or are aligned (Fig. 7d).

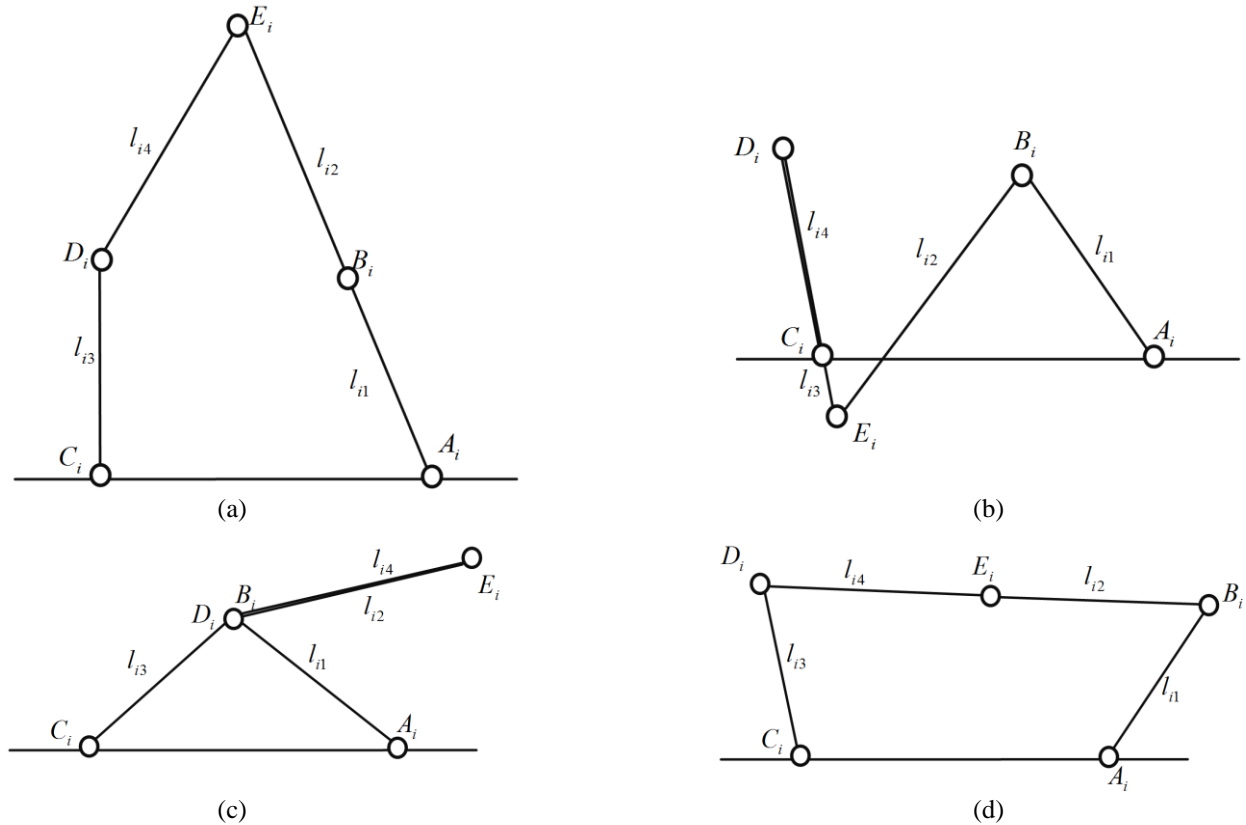


Fig. 7. Singularities in the five-bar mechanism

Thanks to the limit bars on the robot mobile base of restraining all the joint ranges, only the singularity in Fig. 7a is achievable in reality, and occurs when q_{B_i} reach 2π . In this case, the end-effector is close to the circular trajectory originating at A_i with radius $l_{i1} + l_{i2}$ (0.92 m). This dimension is far beyond the diameter of the lower limbs (around 0.20 m), and so this robot will not approach this singularity in practice. Furthermore, a safety mechanism will stop the motors when the robot approaches the singularity region.

6 CONCLUSIONS

A new medical robot, MedRUE, is presented in this paper. It has the ability to diagnose PAD in the large, complex and twisted arterial system of the lower limbs. An intuitive solution for its direct and inverse kinematic model is discussed. Using this method, a complex serial-parallel robot system is decomposed into several simplified sub mechanisms. This system will be proposed to relieve sonographers of their daily physical load of carrying an ultrasound imaging equipment. The robot will not only help in the diagnosis of PAD automatically, but also provide reliable data for 3D reconstruction in future research.

ACKNOWLEDGMENTS

The authors thank the *Fonds québécois de la recherche sur la nature et les technologies*, who provided the funding for this project.

REFERENCES

1. Ouriel, K., "Peripheral arterial disease," *The Lancet*, Vol. 358, No. 9289, pp. 1257-1264, 2001.
2. Sharma, A. M. and Aronow, H. D., *Traditional and Novel Risk Factors in Atherothrombosis*, InTech, 2012.
3. Dormandy, J. A. and Rutherford, R. B., "Management of peripheral arterial disease(PAD)," *Journal of Vascular Surgery*, Vol. 31, No. 1, pp. S1-S296, 2000.
4. Norgren, L. et al., "Inter-Society consensus for the management of peripheral arterial disease," *Journal of Vascular Surgery*, Vol. 45, No. 1, pp. S5-S67, 2007.
5. Arbeille, P. et al., "Echographic examination in isolated sites controlled from an expert center using a 2-D echograph guided by a teleoperated robotic arm," *Ultrasound in Medicine and Biology*, Vol. 29, No. 7, pp. 993-1000, 2003.
6. Vieyres, P. et al., "The TERESA project: from space research to ground tele-echography," *Industrial Robot*, Vol. 30, No. 1, pp. 77-82, 2003.
7. Vieyres, P. et al., *M-Health: Emerging Mobile Health Systems*, Springer US, 2006.
8. Courreges, F., Vieyres, P., and Istepanian R., "Advances in robotic tele-echography services - the OTELO system," Proceedings of the 26th Annual *International Conference of the IEEE/ EMBS*, San Francisco, California, USA, pp. 5371-5374, 2004.
9. British Columbia Ultrasonographer's Society, Healthcare Benefit Trust and Health Sciences Association, *Report on Sonographer's Work, Health & Disability Surver*, British Columbia Ultrasonographer's Society, 1996.
10. Masuda, K. et al., "Three dimensional motion mechanism of ultrasound probe and its application for tele-echography system," Proceedings of the 2001 *IEEE/RSJ International Conference on Intelligent Robots and Systems*, Maui, Hawaii, USA, pp. 1112-1116, 2001.
11. Masuda, K. et al. "Robotic tele-diagnosis system of echography and wireless experiment for mobile telemedicine," Proceedings of the *Second Joint EMBS/BMES Conference*, Houston, Texas, USA, pp. 1855-1856, 2002.
12. Martinelli, T. et al., "Robot-based tele-echography: clinical evaluation of the TER system in abdominal aortic exploration," *Ultrasound in Medicine*, Vol. 26, No. 11, pp. 1611-1616, 2007.
13. Pierrot, F., "Hippocrate: A safe robot arm for medical applications with force feedback," *Medical Image Analysis*, Vol. 3, No. 3, pp. 285-300, 1999.
14. Abolmasesumi, P., "Image-guided control of a robot for medical ultrasound," *IEEE Transactions on Robotics and Automation*, Vol. 18, No. 1, pp. 11-23, 2002.
15. Lessard, S., B. Pascal, and I. A. Bonev, "A new medical parallel robot and its static balancing optimization," *Medical Devices*, Vol. 1, No. 4, pp. 272-278, 2007.
16. Lessard, S., I. Bonev, and P. Bigras, *Parallel Manipulator*, US Patent No 7,673,537, 2010.
17. Lessard, S., *Conception d'un système robotique sécuritaire pour la prise d'images échographiques*, in *Génie de la production automatisée*. 2008, École de technologie supérieure: Montréal. p. 171.
18. Craig, J. J., *Introduction to Robotics: Mechanics and Control*. 3rd ed, Prentice Hall, 2005.